Electronic
Research Archive

Research article

Bifurcation analysis on the reduced dopamine neuronal model

Xiaofang Jiang, Hui Zhou, Feifei Wang, Bingxin Zheng and Bo Lu*

School of Mathematical Science, Henan Institute of Science and Technology, Xinxiang 453003, China

* **Correspondence:** Email: cheersnow@163.com.

Abstract: Bursting is a crucial form of firing in neurons, laden with substantial information. Studying it can aid in understanding the neural coding to identify human behavioral characteristics conducted by these neurons. However, the high-dimensionality of many neuron models imposes a difficult challenge in studying the generative mechanisms of bursting. On account of the high complexity and nonlinearity characteristic of these models, it becomes nearly impossible to theoretically study and analyze them. Thus, this paper proposed to address these issues by focusing on the midbrain dopamine neurons, serving as the central neuron model for the investigation of the bursting mechanisms and bifurcation behaviors exhibited by the neuron. In this study, we considered the dimensionality reduction of a high-dimensional neuronal model and analyzed the dynamical properties of the reduced system. To begin, for the original thirteen-dimensional model, using the correlation between variables, we reduced its dimensionality and obtained a simplified three-dimensional system. Then, we discussed the changing characteristics of the number of spikes within a burst by simultaneously varying two parameters. Finally, we studied the co-dimension-2 bifurcation in the reduced system and presented the bifurcation behavior near the Bogdanov-Takens bifurcation.

Keywords: dopamine neurons; dimensionality reduction; firing rate; inter-spike interval; bifurcation

1. Introduction

The activity of midbrain dopamine neurons, as reflected in levels of extracellular dopamine concentration and the BLOD-fMRI (blood oxygen level dependent functional magnetic resonance imaging, BOLD-fMRI) signals in their target areas, is hypothesized to represent a reward prediction error or confidence in a prediction of a desired outcome [1–3]. Firing patterns of dopamine neurons influence dopamine signaling, for example, electrical stimulation of dopaminergic cells with 40 Hz (Hertz) increased extracellular concentrations of dopamine in the rat striatum more effectively than the same amount of stimulation with 10 Hz [4, 5]. In vitro experiments, dopamine neurons exhibit regular firing with frequency from 1 to 7 Hz [6–9]. However, in living organisms, different

distribution patterns are observed, and these include regular single spiking firing, irregular single spiking firing, and bursting, which are present in both freely moving [10, 11] and anesthetized [12, 13] rats.

Under different conditions, dopamine neurons exhibit a variety of oscillatory patterns. For example, after blocking the spiking with TTX (Tetrodotoxin), the neurons exhibit a slow wave firing that is approximately sinusoidal and calcium-mediated [8, 14, 15]. This oscillation is in the frequency range of the spike. On the other hand, in both in vivo and ex vivo experiments, blocking [16–18] or minimizing [8, 19, 20] the small conductance SK (small conductance calcium activated potassium, SK) potassium channels increases the tendency of the bursting to rhythmic firing rhythms. These bursts usually end in a depolarizing blockade, similar to the bursting seen in rats on long-term antipsychotic drugs [21, 22]. Depolarizing blockage refers to a state in which the resting state of the membrane potential is programmed to support a more depolarization of the active potential generation. Clues to the bursting mechanism include: (1) blocking the spike firing and SK channels and triggering a plateau potential oscillation in the bottom layer [8, 23, 24], during which the depolarization phase can last for several seconds, and (2) L-type calcium channel agonists are also sufficient to trigger bursting behavior. L-type calcium channel-sparing agents disrupt the bursting behavior triggered by the SK channel blockade [25, 26]. The dopamine neuron model proposed by Yu and Canavier [27, 28] is the only model that captures the behavior of the SK channel blocking to mediate bursting in the dopamine neuron. The most notable feature of the model is that the resting phase is more depolarized than the membrane potential during the inter-spike.

In many mathematical models of bursting emanation, the membrane potential has a slow oscillation below, during which the spike of the bursts appear during depolarization, and the inter-spike intervals without emanation are more hyperpolarized than the inter-spike interval, which are often called square-wave bursts [29–32]. A class of anomalous bursting is considered, in which the non-emitting inter-spike intervals are more depolarized than the mean membrane potential observed during the interspike interval. The single atrial compartment model of dopamine neurons studied in this chapter is derived from the model constructed by Yu and Canavier [33, 34].

Due to the complexity of neurons, neuron models are often characterized by high-dimensional complex nonlinear dynamical systems. The research process of a high-dimensional model is very difficult, so we use the method in the literature [35]: a projection method to reduce dimension. The dopamine neuron model studied in this chapter is a 13-dimensional nonlinear dynamical system. The original 3D system simulates the biological properties of the dopamine neuron very well. However, it is very difficult to study the kinetic properties of this model directly. We first use variable correlation to reduce the original 3D model in two steps to obtain a simplified system. Then, we discuss the variation rule of the spikes in the simplified system. By changing the parameters V_{Leak} and g_{Na} simultaneously, it is found that the number of spikes in the simplified model of the action potential varies regularly during a single week, and a number of turbid regions are created. Finally, the birfucation of equilibrium points of the simplified system are studied. The remaining two-dimensional bifurcation of the simplified system, such as the CP bifurcation (cusp bifurcation), the BT bifurcation (Bogdanov-Takens bifurcation), and the GH bifurcation (generalized Hopf bifurcation), are obtained by calculation. A detailed analysis of the topological structure in the vicinity of the BT point is carried out to obtain the specific structure of the bifurcation on the central manifold in the vicinity of the point.

2. Materials and methods

The model presented in this paper is a single-compartment midbrain dopamine neuron (cylinder of diameter $d = 15$ μm and length $L = 25$ μm) described by the following transmembrane potential [33]:

$$C_m \frac{dV}{dt} = -I_{Na} - I_{CaL} - I_{KDR} - I_{KA} - I_{KERG} - I_{KSK} - I_H - I_{Leak} + 0.1 I_s / \pi dL \tag{2.1}$$

where $I_{Na} = g_{Na} m^3 h h_s (V - V_{Na})$ and $I_{CaL} = g_{CaL} l (V - V_{Ca})$ are fast sodium and L-type calcium currents, and $I_{KDR} = g_{KDR} n^3 (V - V_K)$, $I_{KA} = g_{KA} p (q_1/2 + q_2/2)(V - V_K)$, $I_{KERG} = g_{KERG} o (V - V_K)$, $I_{KSK} = g_{KSK}(V - V_K)/(1 + (0.00019/[Ca])^4)$ are delayed rectifier, A-type, ether-a-go-go-related, and small conductance calcium dependent potassium currents, respectively. $I_H = g_H m_H^2 (V - V_H)$ is a nonspecific hyperpolarization-activated cation current and leak current I_{Leak} is comprised of a calcium ion specific component $I_{LCa} = g_{LCa}(V - V_{Ca})$ and a nonspecific component $I_{LNS} = g_{LNS}(V - V_{Leak})$. I_s denotes a small external stimulus current. In this paper, we assume that without the external stimuli, namely, $I_s = 0$, the membrane capacitance $C_m = 1$ μF/cm^2.

The voltage-dependent conductances are described using the Hodgkin-Huxley formalation:

$$\frac{dx}{dt} = \frac{x_\infty - x}{\tau_x}, x = m, h, h_s, n, l, m_H, p, q_1, q_2 \tag{2.2}$$

with $x_\infty = 1/[1 + \exp(-\frac{V - x_{half}}{x_k})]$, in which x_{half} and x_k represent the half-activation voltage and slope of the steady-state Boltzmann fit to x_∞. Time constants:

$$\tau_m = 0.01 + \frac{1}{\frac{15.6504 + 0.4043V}{1 - \exp(-19.565 - 0.50542V)} + 3.0212 \exp(-7.463e - 3V)},$$

$$\tau_h = 0.4 + \frac{1}{5.0754e - 4 \exp(-6.3213e - 2V) + 9.7529 \exp(0.13442V)},$$

$$\tau_{h_s} = 20 + \frac{580}{1 + \exp(V)},$$

$$\tau_n = \frac{22.7165}{1 + \exp(-\frac{V + 61.1253}{4.4429})}[\frac{1}{1 + \exp(\frac{V + 36.8869}{9.7083})} + 0.0052] + 0.7397,$$

$$\tau_l = \frac{1}{\frac{0.020876(V + 39.726)}{1 - \exp(-\frac{V + 39.726}{4.711})} + 0.19444 \exp(-\frac{V + 15.338}{224.21})},$$

$$\tau_{m_H} = 26.21 + \frac{3136}{1 + \exp(-\frac{V + 22.686}{29.597})},$$

$$\tau_p = \frac{95.5813}{1 + \exp(-\frac{V + 71.5402}{26.0594})}[\frac{1}{1 + \exp(\frac{V + 62.5026}{6.5199})} - 0.5108] + 48.2438,$$

$$\tau_{q_1} = 6.1 \exp(0.015V),$$

$$\tau_{q_2} = 294.0087 + \frac{55.8321}{1 + \exp(\frac{V - 84.8594}{35.3239})}[\frac{1}{1 + \exp(\frac{V + 52.5933}{4.9104})} - 5.2348].$$

The current I_{KERG} uses a kinetic scheme described previously [33]. The current description requires following two differential equations:

$$\frac{do}{dt} = \alpha_o(1 - o - i) + \beta_i i - o(\alpha_i + \beta_o), \tag{2.3}$$

$$\frac{di}{dt} = \alpha_i o - \beta_i i, \tag{2.4}$$

where o and i represent the fraction of ERG (Ether-a-go-go-RelatedGene) channels in the open and inactivated states, and $\alpha_o, \beta_o, \alpha_i, \beta_i$ denote the corresponding reaction rates:

$$\begin{aligned}
\alpha_o &= 0.0036 \exp(0.0759V), \\
\beta_o &= 1.2523e - 5 \exp(-0.0671V), \\
\alpha_i &= 91.11 \exp(0.1189V), \\
\beta_i &= 12.6 \exp(0.0733V).
\end{aligned}$$

The Ca^{2+} balance is described by:

$$\frac{d[Ca]}{dt} = -2 f_{Ca}(I_{LCa} + I_{Cap} + I_{CaL})/(Fd), \tag{2.5}$$

where $[Ca]$ denotes the Ca^{2+} concentration in mM (mM/L), and $f_{Ca} = 0.018$ and F are the fraction of the unbuffered free calcium and Faraday constant. I_{Cap} represents extrusion of Ca^{2+}, which is modeled by a non-electrogenic pump:

$$I_{Cap} = I_{Capmax}/(1 + 0.0005/[Ca]),$$

where $I_{Capmax} = 11 \ \mu A/cm^2$.

The parameters for each current are listed in Table 1.

Table 1. Parameter values for the dopamine neuron model.

Maximal conductances ($\mu S/cm^2$)	$g_{CaL} = 139$, $g_{KDR} = 1117$, $g_{KA} = 1680$, $g_{KSK} = 70$, $g_{Na} = 6000$, $g_{KERG} = 130$, $g_H = 78$, $g_{LNS} = 280$, $g_{LCa} = 2.45$
Reversal potentials (mV)	$V_{Na} = 60$, $V_{Ca} = 50$, $V_K = -90$, $V_H = -29$, $V_{Leak} = -65$
Half-activation voltages (mV)	$m_{half} = -30.09$, $h_{half} = -54$, $h_{shalf} = -54.8$, $n_{half} = -25$, $l_{half} = -45$, $m_{Hhalf} = -77.6$, $p_{half} = -35.1$, $q_{1half} = q_{2half} = -80$
Slopes (mV)	$m_k = 13.2$, $h_k = -12.8$, $h_{sk} = -1.57$, $n_k = 12$, $l_k = 7.5$, $m_{Hk} = -17.317$, $p_k = 13.4$, $q_{1k} = q_{2k} = -6$

Simulations and dimensionality reduction for the original 13-dimensional single-compartment model was performed using the NEURON software [36], and data processing was conducted using ORIGIN [37] and MATLAB softwares [38]. The bifurcation diagrams for the slow plateau potential was calculated with XPPAUT. The bifurcation diagrams for the reduced three-dimensional system were generated by the MATCONT package [39].

3. Results

3.1. Model reduction

Combined Eqs (2.1)–(2.5) obtaining the original 13-dimensional model, using the formulas and parameters in Section 2, simulated the discharge properties of the original model; for specifics, see references [33].

Given the dimension reduction experience of the Hodgkin-Huxley model, the four-dimensional reduced to three-dimensional, see references [35, 40]. To start, consider the alternative method with the appropriate variable reduced dimensionality.

In order to better hold and explore the firing properties of the original model, this paper adopts two-step dimensionality reduction. The first step is reduced to eight-dimension and keeps the firing characteristics of the original model; in order to be convenient for dynamic analysis of the reduced model, the second step is reduced to three-dimensional.
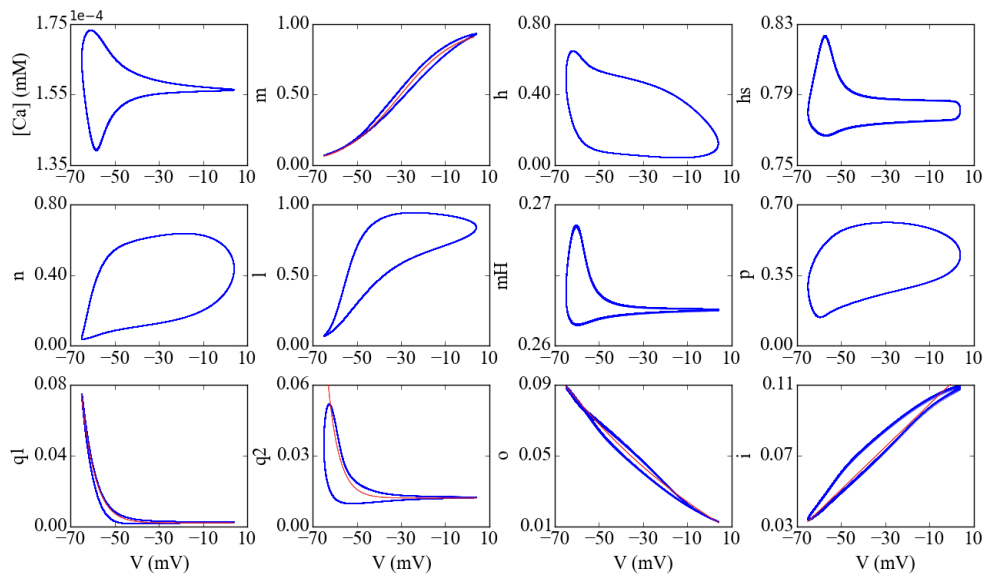

Figure 1. Phase portraits of gating variables and membrane potential. Red lines are the corresponding fitted curves (m, q_1, q_2, o, i).

Step one: Use membrane potential dimensionality reduction. Based on the initial parameters of the original model, draw a phase portrait of each variable and membrane potential (Figure 1). As can be seen from Figure 1, gating variables m, q_1, q_2, o, i are closely related to membrane potential, but others have no significant relationship. Utilizing software ORIGIN curve fitting can be drawn:

$$
\begin{aligned}
m &= 0.91149 + 0.00724V - 3.35746e-4V^2 - 3.81279e-6V^3, \\
q_1 &= \exp(-12.87201 - 0.15835V), \\
q_2 &= 0.0125 + 1.7482e-7\exp(-0.19914V), \\
o &= 0.01527 - 7.54913e-4V + 5.86583e-6V^2, \\
i &= 0.11024 + 0.00119V.
\end{aligned}
$$

Take these five variables into the original equation reduced to the 8-dimensional model. In order to make discharge properties of the 8-dimensional reduced model consistent with the original model, we adjust $g_{Na} = 5400\ \mu S/cm^2$, $V_K = -85\ mV$ (Millivolt), and other parameters remain unchanged. As can be seen from Figure 2, when spiking, firing properties of the 8-dimensional model and the original model are almost exactly the same (frequency and amplitude). $g_{KSK} = 0$, the original model appears

bursting; $g_{KSK} = 17.905 \, \mu S/cm^2$, the 8-dimensional model appears bursting, which is consistent with the original model (frequency, period, duty cycle).
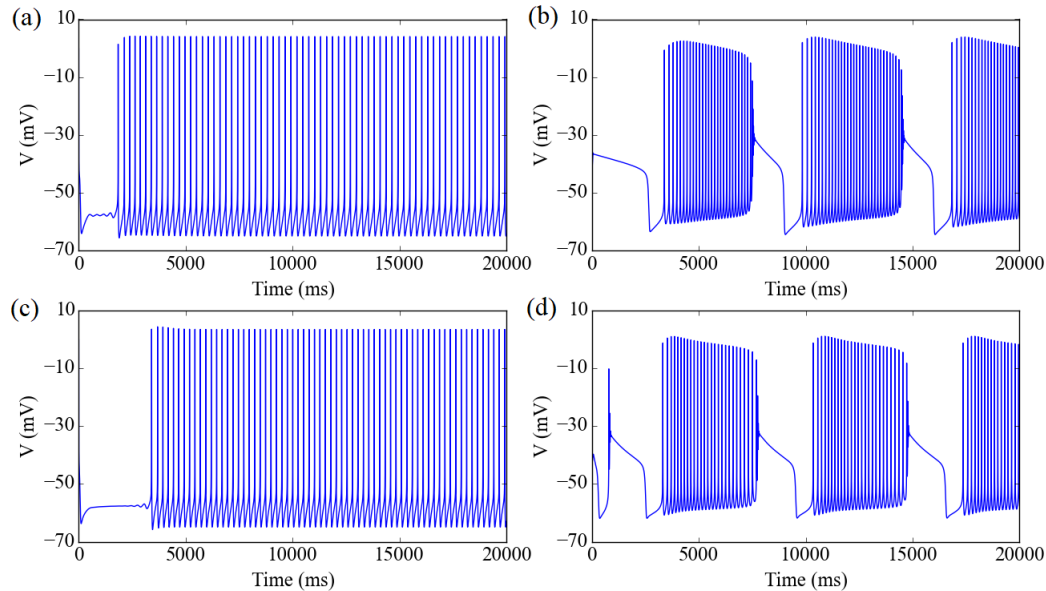
Figure 2. Firing patterns of the original model and 8-dimensional model. (a) spiking of the original model with $g_{KSK} = 0 \, \mu S/cm^2$, the frequency is 3 Hz; (b) bursting of the original model with $g_{KSK} = 0 \, \mu S/cm^2$, the period is 6.98 S, the Duty ratio is 0.65; (c) spiking of the the 8-dimensional model with $g_{KSK} = 17.905 \, \mu S/cm^2$, the frequency is 4 Hz; (d) bursting of the the 8-dimensional model with $g_{KSK} = 17.905 \, \mu S/cm^2$, the period is 6.72 S, the Duty ratio is 0.61;

Step two: Use gating variables n and $[Ca]$ dimensionality reduction. Similar to the first step, draw a phase portrait of remaining variables and n or $[Ca]$. It can be seen from phase portraits, gating variables h, l, p strongly depends on n, and h_s, m_H depends on $[Ca]$. Similarly, it can be obtained by curve fitting:

$$
\begin{aligned}
h &= 0.74295 - 3.39187n + 6.43961n^2 - 4.51583n^3, \\
l &= 0.083 + 0.1n + 2.1n^2, \\
p &= 0.1 + 1.8n - 3n^2 + 2.3n^3, \\
h_s &= 7.78317 - 120581.5037[Ca] + 6.96398e - 8[Ca]^2 - 1.35265e - 12[Ca]^3, \\
m_H &= 0.26401 - 4.19362e - 6\exp(41537.6367[Ca]).
\end{aligned}
$$

Take these five variables into the 8-dimensional model and obtain a reduced three-dimensional system as follows:

$$\begin{cases} \dfrac{dV}{dt} = \dfrac{1}{C_m}(-I_{Na} - I_{CaL} - I_{KDR} - I_{KA} - I_{KERG} - I_{KSK} - I_H - I_{Leak}), \\ \dfrac{dn}{dt} = \dfrac{n_\infty - n}{\tau_n}, \\ \dfrac{d[Ca]}{dt} = \dfrac{-2f_{Ca}(I_{LCa} + I_{Cap} + I_{CaL})}{Fd}, \end{cases} \quad (3.1)$$

where specific ion channel models are shown above.

In order to better explore dynamic properties of the system Eq (3.1), adjust parameters $I_{Capmax} = 21\,\mu A/cm^2$, $g_{Na} = 6000\,\mu S/cm^2$ (the original value), $g_{CaL} = 60\,\mu S/cm^2$, $g_{KDR} = 17\,\mu S/cm^2$, and other parameters remain unchanged.

3.2. Influence of two-parameter on firing pattern

First, we consider the impact of parameter changes on the firing pattern of the three-dimensional system. By examining the system's firing patterns under various parameters, it is found that they are essentially similar. In this paper, we select the parameters V_{Leak} and g_{Na}, and observe the changes in the firing pattern of the simplified model as the parameters change. By statistically analyzing the number of peaks within a single cluster for each combination of V_{Leak} and g_{Na} parameters, we obtain the distribution of the number of spikes within a single burst of the system's firing on a two-dimensional plane (V_{Leak}, g_{Na}) (Figure 3).
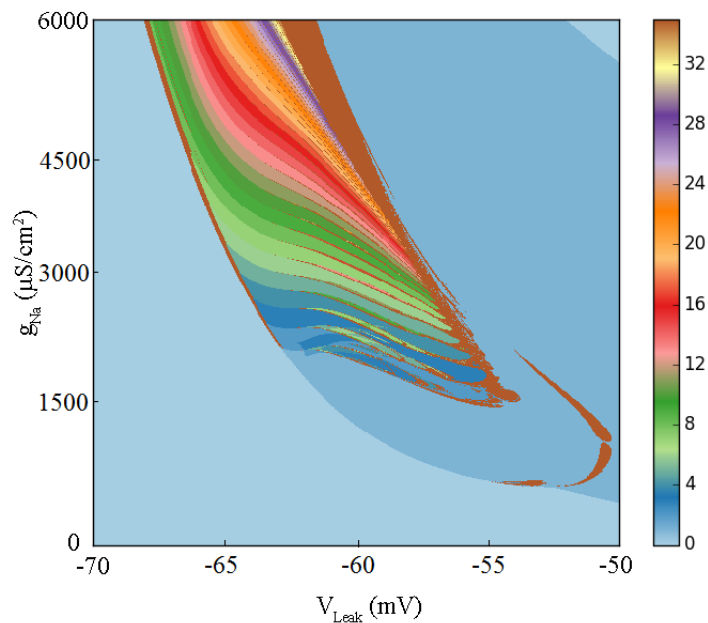
Figure 3. Spike-counting diagram with two-parameter V_{Leak} and g_{Na}. The color bar in the right column shows the number of spikes within a burst. The number of 0 signifies no firing; the number 1 represents spiking; the number 2–34 indicates regular bursting, while the number 35 denotes chaotic bursting.

Figure 3 shows the transient pattern of the discharge mode of the system with the change of g_{Na} and V_{Leak}. In Figure 3, the horizontal and vertical axes are g_{Na} and V_{Leak}, with values ranging from -70 to -50 mV and 0–6000 μS/cm^2, respectively. From Figure 3, it can be seen that with the increase of the parameters, the system exhibits a firing pattern from resting to spiking, then to bursting, and finally to resting again. The different colors in Figure 3 represent the number of spikes in a single burst, and the specific number of spikes indicated by each color is shown on the right side of the ribbon marking the value, in which the light blue color marked with 0 represents that the system is not firing, 1 represents that the peaks are spiking, 2–34 represents that the system is in the regular bursting state at this time, and 35 indicates that the system enters into a chaotic bursting state. When $V_{Leak} = -58$ mV, with the increase of g_{Na}, when $g_{Na} > 1850$ μS/cm^2, the system shows a regular additive period firing phenomenon, the number of spikes in a single burst starts to increase gradually from 2, and the different numbers of regions are separated by the chaotic region, which means that each time the number of peaks changes, the system has to go through a chaotic region. Therefore, the 'comb' shaped chaotic region can be clearly seen in Figure 3. In addition, the system also generates three chaotic regions around V_{Leak} values of -55 to -54, -52 to -51 mV, and values of g_{Na} are from 1000 to 2000 μS/cm^2, and there is also a conical chaotic region between values of V_{Leak} from -63 to -55 mV and g_{Na} values of 2000 to 6000 μS/cm^2.
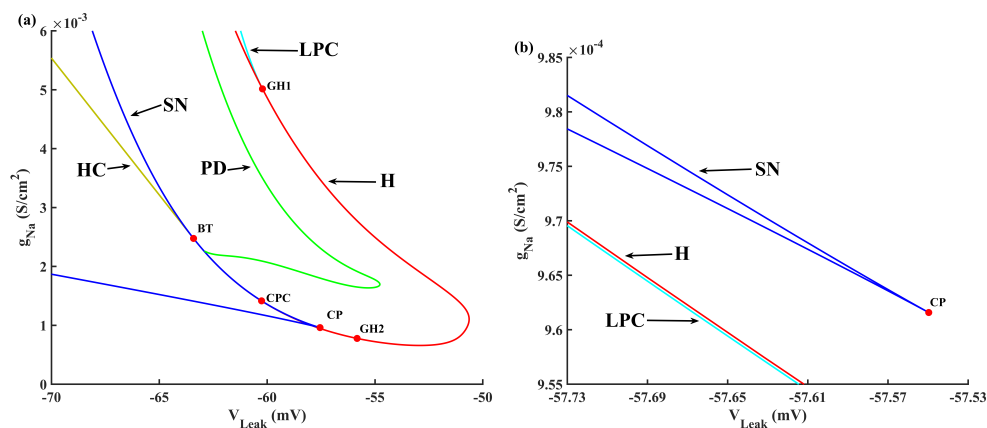

Figure 4. Two-parameter (V_{Leak}, g_{Na}) bifurcation diagram of the oscillatory regime. (a) Global view; (b) a partial amplification of panel (a). The blue curve, SN, corresponds to the saddle-node bifurcation. The red curve H marks the Hopf bifurcation curve. The green curve PD denotes the different period-doubling bifurcation curves of different limit cycle, the yellow curve HC denotes the homoclinic bifurcation curve, the light blue LPC curve denotes the folding bifurcation curve of the limit cycle, the CP point denotes the Cusp bifurcation, the BT point denotes the Bogdanov-Takens bifurcation, the GH1 and GH2 points denote the Generalized Hopf bifurcation, and the CPC denotes the Cusp bifurcation of the limit cycle.

Second, we branch out to system Eq (3.1). On the basis of dimensionality reduction, we select the two parameters V_{Leak} and g_{Na} above for the co-dimension-2 bifurcation analysis, and the results are shown in Figure 4. Figure 4(a) shows the co-dimension-2 bifurcation diagrams for the values of V_{Leak} in the range of $[-70, 50]$ mV and g in the range of $[0, 6000]$ μS/cm^2. Figure 4(b) is a localized enlargement of Figure 4(a). From Figure 4(a), it can be seen that the system exhibits a rich variation of

equilibrium points as the parameters are varied. From the figure, it can be seen that the co-dimension-2 bifurcation points of the system appear in CP $(-57.549678, 961.58291)$, BT $(-63.413152, 2476.1036)$, GH1 $(-60.217081, 5015.182)$, and GH2 $(-55.831514, 778.22531)$, respectively.
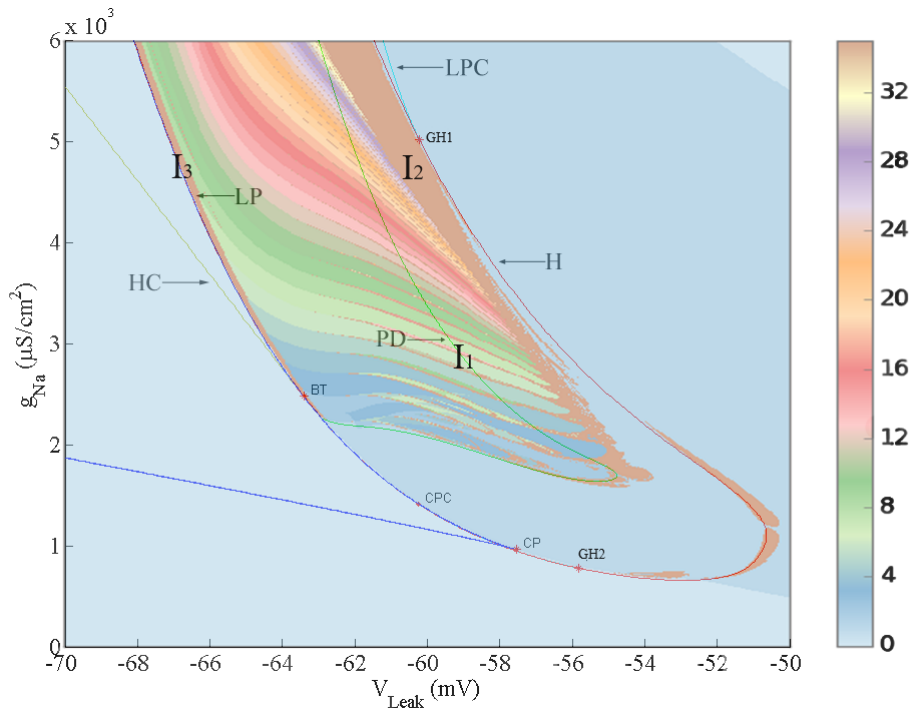
Figure 5. Influence of two-parameter on firing pattern.

Then, we superimpose Figure 3 on Figure 4 to investigate the effect of system bifurcation on the firing behavior, and the results are shown in Figure 5. It can be seen that the chaotic region I_1 is formed by the PD bifurcation, because when the system generates PD bifurcation, the PD cascade is formed by it. With the increase of V_{Leak}, another chaotic region I_2 is formed when the system passes through the LPC, and with the decrease of parameter V_{Leak}, I_3 region is formed when the system passes through the H-curve. As can be seen from Figure 5, when the system passes through the Hopf bifurcation curve from resting to spiking, the system changes from a resting state to a firing state, and the system starts the firing behavior; when the system passes through the PD curve, the spiking changes to a bursting state; and when the system passes through the H curve from left to right, the system transitions to either a resting or a spiking state.

Figure 6 uses the bifurcation diagram of the sequence of the inter-spike interval to further delineate the change of the firing behavior of the system. Figure 6(a) presents the firing pattern of the system exhibiting a PD bifurcation when $V_{Leak} = -58$ mV, Figure 6(b) shows the adding-period bifurcation related to g_{Na}, and Figure 6(c) shows the maximum Lyapunov exponent. It is seen that the system exhibits the formation of chaotic region from the PD bifurcation with the increase of g, which corresponds well to the maximum Lyapunov exponent. Figure 6(d) is a local enlargement of Figure 6(a), which shows a clearer bifurcation of the PD bifurcation phenomenon.
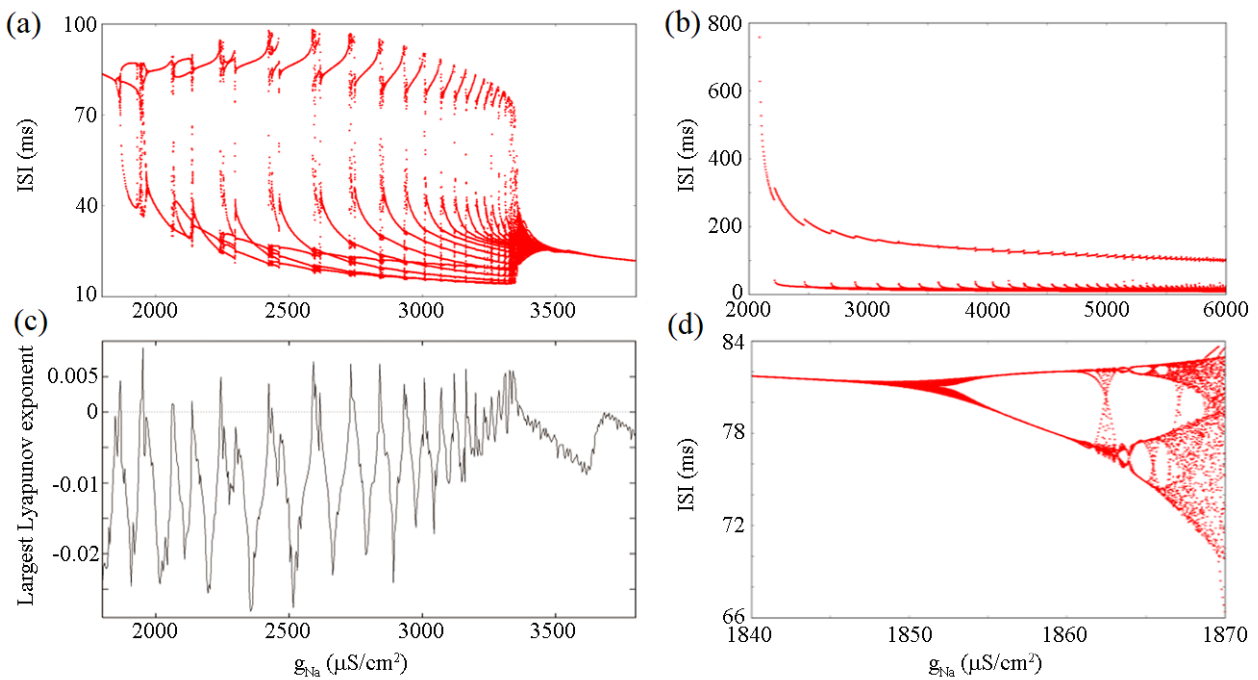
Figure 6. ISI (interspike interval) bifurcation diagram versus g_{Na}. (a) The PD bifurcation diagram; (b) adding PD diagram; (c) the largest Lyapunov exponent corresponding PD bifurcation diagram in panel (a); (d) the partial enlargement of the PD bifurcation diagram in panel(a).

3.3. Bifurcation analysis

The Bogdanov-Takens bifurcation point BT appears when $(V_{Leak}, g_{Na})^T = (-63.413152, 2476.1036)^T \triangleq \mu_0$, with corresponding equilibrium coordinate $(V, n, [Ca])^T = (-56.177560, 0.069258865, 0.000022315168)^T \triangleq X_0$. Rewrite the system Eq (3.1) as:

$$\frac{dX}{dt} = F(X, \mu) = \begin{pmatrix} f_1(X, \mu) \\ f_2(X, \mu) \\ f_3(X, \mu) \end{pmatrix},$$

where $X = (V, n, [Ca])^T$, $\mu = (V_{Leak}, g_{Na})^T$, and

$$
\begin{aligned}
f_1(X, \mu) &= -\frac{1}{C_m}(I_{Na} + I_{CaL} + I_{KDR} + I_{KA} + I_{KERG} + I_{KSK} + I_H + I_{Leak}), \\
f_2(X, \mu) &= \frac{n_\infty - n}{\tau_n}, \\
f_3(X, \mu) &= \frac{-2f_{Ca}(I_{LCa} + I_{Cap} + I_{CaL})}{Fd}.
\end{aligned}
$$

Consider the Taylor series of $F(X, \mu)$ around (X_0, μ_0):

$$F(X, \mu) = DF(X_0, \mu_0)(X - X_0) + F_\mu(X_0, \mu_0)(\mu - \mu_0)$$

$$+ \frac{1}{2}D^2 F(X_0, \mu_0)(X - X_0, X - X_0) + F_{\mu X}(X_0, \mu_0)(\mu - \mu_0)(X - X_0) + \cdots.$$

Note matrix

$$A \triangleq DF(X_0, \mu_0) = \left(\begin{array}{ccc} \frac{\partial f_1}{\partial V} & \frac{\partial f_1}{\partial n} & \frac{\partial f_1}{\partial [Ca]} \\ \frac{\partial f_2}{\partial V} & \frac{\partial f_2}{\partial n} & \frac{\partial f_2}{\partial [Ca]} \\ \frac{\partial f_3}{\partial V} & \frac{\partial f_3}{\partial n} & \frac{\partial f_3}{\partial [Ca]} \end{array} \right) \Bigg|_{(X_0, \mu_0)}$$

$$= \left(\begin{array}{ccc} 0.0362113781 & -6.139680873 & -25231.15614 \\ 0.0003385368880 & -0.06302066178 & 0 \\ -2.101106203 \times 10^{-9} & 6.191978014 \times 10^{-7} & -0.009570132519 \end{array} \right),$$

$$F_\mu(X_0, \mu_0) = \left(\begin{array}{cc} \frac{\partial f_1}{\partial V_{Leak}} & \frac{\partial f_1}{\partial g_{Na}} \\ \frac{\partial f_2}{\partial V_{Leak}} & \frac{\partial f_2}{\partial g_{Na}} \\ \frac{\partial f_3}{\partial V_{Leak}} & \frac{\partial f_3}{\partial g_{Na}} \end{array} \right) \Bigg|_{(X_0, \mu_0)} = \left(\begin{array}{cc} 0.28 & 0.0006022539009 \\ 0 & 0 \\ 0 & 0 \end{array} \right).$$

The matrix A has three eigenvalues, that is, 0, 0, and -0.0363794162. Let $P = (p_1, p_2, p_0)$ be an invertible matrix, which satisfies $P^{-1}AP = J$, where $J = \left(\begin{array}{cc} J_0 & 0 \\ 0 & J_1 \end{array} \right)$, $J_1 = -0.0363794162$, p_1 and p_2 are generalized eigenvectors of the matrix A corresponding to the double-zero eigenvalues, and p_0 contains the generalized eigenvectors of the matrix J_1. We have

$$\begin{aligned} p_1 &= (1, 0.005371826285, 1.280151594 \times 10^{-7})^T, \\ p_2 &= (1, -0.07986728884, -0.00001876357667)^T, \\ p_0 &= (78.69525161, 1, -0.0000169288641)^T. \end{aligned}$$

If $P^{-1} = (q_1, q_2, q_0^T)^T$, then

$$\begin{aligned} q_1 &= (1.523089493, -110.5217903, 5.516093986 \times 10^5)^T, \\ q_2 &= (0.01657847663, -2.044581349, -43708.42341)^T, \\ q_0 &= (-0.006857694193, 1.430408689, -6454.023143). \end{aligned}$$

By calculating expressions (28) and (29) in [41], then we obtain

$$\begin{aligned} a &= \frac{1}{2}p_1^T(q_2 \cdot D^2 F(X_0, \mu_0))p_1 = 0.0003695666038, \\ b &= p_1^T(q_1 \cdot D^2 F(X_0, \mu_0))p_1 + p_1^T(q_2 \cdot D^2 F(X_0, \mu_0))p_2 = 0.07459975788, \end{aligned}$$

$$\begin{aligned} S_1 &= F_\mu^T(X_0, \mu_0)q_2 = (0.004641973456, 0.000009984452221)^T, \\ S_2 &= \left[\frac{2a}{b}(p_1^T(q_1 \cdot D^2 F(X_0, \mu_0))p_2 + p_2^T(q_2 \cdot D^2 F(X_0, \mu_0))p_2) \right. \end{aligned}$$

$$-p_1^T(q_2 \cdot D^2 F(X_0, \mu_0))p_2 \Big] F_\mu^T(X_0, \mu_0)q_1$$

$$-\frac{2a}{b} \sum_{i=1}^{2} (q_i \cdot (F_{\mu X}(X_0, \mu_0) - ((p_0 J_1^{-1} q_0)F_\mu(X_0, \mu_0))^T \times D^2 F(X_0, \mu_0)))p_i$$

$$+(q_2 \cdot (F_{\mu X}(X_0, \mu_0) - ((p_0 J_1^{-1} q_0)F_\mu(X_0, \mu_0))^T \times D^2 F(X_0, \mu_0)))p_1$$

$$= (-16887.39227, -1.949460563 \times 10^6)^T.$$

If we choose λ_1 and λ_2 as bifurcation parameters, where $\lambda_1 = V_{Leak} + 63.413152$, $\lambda_2 = g_{Na} - 2476.1036$, then

$$\begin{aligned}
\beta_1 &= S_1^T(\mu - \mu_0) = 0.004641973456\lambda_1 + 0.000009984452221\lambda_2, \\
\beta_2 &= S_2^T(\mu - \mu_0) = -16887.39227\lambda_1 - 1.949460563 \times 10^6 \lambda_2.
\end{aligned}$$

Using the Theorem 1 in [41], the reduced system (6) near (X_0, μ_0) is locally topologically equivalent to

$$\begin{cases}
\dfrac{dz_1}{dt} = z_2, \\
\dfrac{dz_2}{dt} = \beta_1 + \beta_2 z_1 + az_1^2 + bz_1 z_2 \\
\qquad = 0.004641973456\lambda_1 + 0.000009984452221\lambda_2 \\
\qquad\quad +(-16887.39227\lambda_1 - 1.949460563 \times 10^6 \lambda_2)z_1 \\
\qquad\quad +0.0003695666037z_1^2 + 0.07459975786z_1 z_2.
\end{cases} \quad (3.2)$$

Further, using a coordinate transformation and time reparametrization

$$\begin{aligned}
t &= \frac{b}{a}t_1 = \frac{0.07459975786}{0.0003695666037}t_1, \\
z_1 &= \frac{a}{b^2}\eta_1 = \frac{0.0003695666037}{(0.07459975786)^2}\eta_1, \\
z_2 &= sign(\frac{b}{a})\frac{a^2}{b^3}\eta_2 = \frac{(0.0003695666037)^2}{(0.07459975786)^3}\eta_2,
\end{aligned}$$

system Eq (3.2) becomes

$$\begin{cases}
\dfrac{d\eta_1}{dt_1} = \eta_2, \\
\dfrac{d\eta_2}{dt_2} = \bar\beta_1 + \bar\beta_2 \eta_1 + \eta_1^2 + s\eta_1\eta_2,
\end{cases}$$

where

$$\begin{aligned}
\bar\beta_1 &= \frac{b^4}{a^3}\beta_1 = 2848.224171\lambda_1 + 6.126264706\lambda_2, \\
\bar\beta_2 &= \frac{b^2}{a^2}\beta_2 = -6.881006842 \times 10^8 \lambda_1 - 7.943352803 \times 10^{10}\lambda_2, \\
s &= sign(ab) = 1.
\end{aligned}$$

Since

$$4\bar{\beta}_1 - \bar{\beta}_2^2 \Longleftrightarrow \lambda_1 + 0.002150906789\lambda_2 - 4.155945278 \times 10^{13}\lambda_1^2$$
$$- 9.595148018 \times 10^{15}\lambda_1\lambda_2 - 5.538262614 \times 10^{17}\lambda_2^2 = 0,$$

$$\bar{\beta}_1 = 0 \Longleftrightarrow \lambda_1 = -0.002150906789\lambda_2,$$
$$\bar{\beta}_2 < 0 \Longleftrightarrow \lambda_1 + 115.4388157\lambda_2 > 0,$$

$$\bar{\beta}_1 + \frac{6}{25}\bar{\beta}_2^2 = o(\bar{\beta}_2^2) \Longleftrightarrow \lambda_1 + 0.002150906789\lambda_2 + 3.989707465 \times 10^{13}\lambda_1^2$$
$$+ 9.211342093 \times 10^{15}\lambda_1\lambda_2 + 5.316732107 \times 10^{17}\lambda_2^2$$
$$= o(|\lambda_1, \lambda_2|^2).$$

According to the theory on the BT bifurcation in [42] and the preceding analysis, we have the following.

Theorem 3.1. *Let* $\lambda_1 = V_{Leak} + 63.413152$ *and* $\lambda_2 = g_{Na} - 2476.1036$. *If bifurcation parameters* (V_{Leak}, g_{Na}) *vary around* $(-63.413152, 2476.1036)$, *then the system (6), at the Bogdanov-Takens bifurcation point BT, is locally topologically equivalent to the following system:*

$$\begin{cases} \dfrac{d\eta_1}{dt_1} = \eta_2, \\ \dfrac{d\eta_2}{dt_2} = 2848.224171\lambda_1 + 6.126264706\lambda_2 \\ \qquad + (-6.881006842 \times 10^8\lambda_1 - 7.943352803 \times 10^{10}\lambda_2)\eta_1 + \eta_1^2 + \eta_1\eta_2. \end{cases} \tag{3.3}$$

System (8) has the following local representation of bifurcation curves in a small neighborhood of the origin:

(1) There is a fold bifurcation curve

$$SN = \{(\lambda_1, \lambda_2) : \lambda_1 + 0.002150906789\lambda_2 - 4.155945278 \times 10^{13}\lambda_1^2$$
$$- 9.595148018 \times 10^{15}\lambda_1\lambda_2 - 5.538262614 \times 10^{17}\lambda_2^2 = 0\};$$

(2) There is a nondegenerate Hopf-bifurcation curve

$$H = \{(\lambda_1, \lambda_2) : \lambda_1 = -0.002150906789\lambda_2, \lambda_1 + 115.4388157\lambda_2 > 0\};$$

(3) There is a saddle homoclinic-bifurcation curve

$$HL = \{(\lambda_1, \lambda_2) : \lambda_1 + 0.002150906789\lambda_2 + 3.989707465 \times 10^{13}\lambda_1^2$$
$$+ 9.211342093 \times 10^{15}\lambda_1\lambda_2 + 5.316732107 \times 10^{17}\lambda_2^2$$
$$= o(|\lambda_1, \lambda_2|^2), \lambda_1 + 115.4388157\lambda_2 > 0\}.$$

In Section 3.3, we conduct a bifurcation analysis of the model, with a specific focus on the BT bifurcation of the system. Through calculations on the simplified model, we obtain an in-depth analysis of the opening and breaking behavior associated with the BT bifurcation. Furthermore, we clarify the topological structure near the bifurcation point, particularly by calculating the homoclinic orbit curve and resolving issues related to its computation.

4. Discussion and conclusions

In this paper, the kinetic properties of a class of dopamine neurons were investigated and abundant results were obtained. Due to the complexity of neurons, neuronal models are often characterized by high latitude and high complexity. We mainly focused on the dynamical properties of high-dimensional systems squeezing a reduced dimensional system. It is very difficult to study the dynamics of the model directly, so we first use the correlation of variables to downsize the original system in two steps and obtain a simplified system in three dimensions.

The first step is to consider the dimensionality reduction using the membrane potential. By drawing the phase diagram of each gating variable with respect to the membrane potential and substituting the appropriate data fitting, a simplified system in eight dimensions is obtained and the system retains the characteristic properties of the original system. The second step of dimensionality reduction is carried out with the help of the gating variables of the potassium channel n, and the calcium concentration $[Ca]$ to obtain the simplified model in three dimensions. It can be seen that the chaotic regions are generated due to the PD bifurcation, and the SN bifurcation on the LPC. Then, we study the equilibrium bifurcation of the system on the basis of a simplified model. The CP bifurcation, BT bifurcation, GH bifurcation, and other residual co-dimension-2 bifurcations of the simplified system are obtained through computation, the topology near the BT bifurcation is analyzed in detail, and the specific structure of each bifurcation on the central manifold near the neighborhood of this point is obtained.

To sum up, we give a method to study a high-dimensional nonlinear neuron model, and by comparing the action potentials generated by the model before and after simplification (the model after the second step of dimensionality reduction loses the firing characteristics of the original model), it is found that the chaotic regions are generated by the cascade formation of PD bifurcation generated by PD bifurcation (Figure 5, $V_{Leak} = [-60, -54]$ mV), and the chaotic regions generated by SN bifurcation on the LPC ($V_{Leak} = [-56, -54]$ mV). The inter-spike interval of the membrane potential of the system is studied to characterize the process of chaos generated by the PD cascade at $V_{Leak} = 58$ mV. However, there is no further comparison of these differences in the generation of chaos, which can be further investigated. In addition, although the article gives the reason for the generation of chaos by combining co-dimension-2 bifurcation, it is difficult to analyze the dynamics of the original high-dimension neuron model, and the generality of the model simplification needs to be further proved.

Use of AI tools declaration

The authors declare they have not used Artificial Intelligence (AI) tools in the creation of this article.

Acknowledgements

Conflict of interest

The authors declare there is no conflicts of interest.

References

1. Y. U. Ying, X. M. Wang, Q. S. Wang, Q. Y. Wang, A review of computational modeling and deep brain stimulation: Applications to Parkinson's disease, *Appl. Math. Mech.*, **41** (2020), 1747–1768. https://doi.org/10.1007/s10483-020-2689-9

2. C. J. Chen, F. H. Min, J. M. Cai, H. Bao, Memristor synapse-driven simplified Hopfield neural network: Hidden dynamics, attractor control, and circuit implementation, *IEEE Trans. Circuits Syst. I*, **71** (2024), 2308–2319. https://doi.org/10.1109/TCSI.2024.3349451

3. F. H. Min, J. Zhu, Y. Z. Cheng, Y. Y. Xu, Dynamical analysis of a tabu learning neuron through the discrete implicit mapping method, *Chaos Solitons Fractals*, **181** (2024), 114716. https://doi.org/10.1016/j.chaos.2024.114716

4. R. M. Wightman, J. B. Zimmerman, Control of dopamine extracellular concentration in rat striatum by impulse flow and uptake, *Brain Res. Rev.*, **15** (1990), 135–144. https://doi.org/10.1016/0165-0173(90)90015-G

5. D. J. Vidyadhara, M. Somayaji, N. Wade, B. Yücel, H. Zhao, N. Shashaank, et al., Dopamine transporter and synaptic vesicle sorting defects underlie auxilin-associated Parkinson's disease, *Cell Press*, **42** (2023), 112231. https://doi.org/10.1016/j.celrep.2023.112231

6. A. A. Grace, S. P. Onn, Morphology and electrophysiological properties of immunocytochemically identified rat dopamine neurons recorded in vitro, *J. Neurosci.*, **9** (1989), 3463–3481. https://doi.org/10.1523/JNEUROSCI.09-10-03463.1989

7. Q. Shan, Y. Tian, H. Chen, X. Lin, Y. Tian, Reduction in the activity of VTA/SNc dopaminergic neurons underlies aging-related decline in novelty seeking, *Commun. Biol.*, **6** (2023), 1224. https://doi.org/10.1038/s42003-023-05571-x

8. H. X. Ping, P. D. Shepard, Apamin-sensitive Ca(2+)-activated K+ channels regulate pacemaker activity in nigral dopamine neurons, *Neuroreport*, **7** (1996), 809–814. https://doi.org/10.1097/00001756-199602290-00031

9. C. J. Knowlton, T. I. Ziouziou, N. Hammer, J. Roeper, C. C. Canavier, Inactivation mode of sodium channels defines the different maximal firing rates of conventional versus atypical midbrain dopamine neurons, *PLOS Comput. Biol.*, **17** (2021), e1009371. https://doi.org/10.1371/journal.pcbi.1009371

10. B. I. Hyland, J. N. J. Reynolds, J. Hay, C. G. Perk, R. Miller, Firing modes of midbrain dopamine cells in the freely moving rat, *Neuroscience*, **114** (2002), 475–492. https://doi.org/10.1016/S0306-4522(02)00267-1

11. G. Hernandez, W. M. Kouwenhoven, E. Poirier, K. Lebied, D. Lévesque, P. P. Rompré, Dorsal raphe stimulation relays a reward signal to the ventral tegmental area via GluN2C NMDA receptors, *PLoS One*, **18** (2023), e0293564. https://doi.org/10.1371/journal.pone.0293564

12. C. R. Lee, E. D. Abercrombie, J. M. Tepper, Pallidal control of substantia nigra dopaminergic neuron firing pattern and its relation to extracellular neostriatal dopamine levels, *Neuroscience*, **129** (2004), 481–489. https://doi.org/10.1016/j.neuroscience.2004.07.034

13. F. Arencibia-Albite, C. A. Jiménez-Rivera, Computational and theoretical insights into the homeostatic response to the decreased cell size of midbrain dopamine neurons, *Physiol. Rep.*, **9** (2021), e14709. https://doi.org/10.14814/phy2.14709

14. Y. Kang, S. T. Kitai, Calcium spike underlying rhythmic firing in dopaminergic neurons of the rat substantia nigra, *Neurosci. Res.*, **18** (1993), 195–207. https://doi.org/10.1016/0168-0102(93)90055-U

15. D. E. Cobb-Lewis, L. Sansalone, Z. M. Khaliq, Contributions of the sodium leak channel NALCN to pacemaking of medial ventral tegmental area and substantia nigra dopaminergic neurons, *J. Neurosci.*, **43** (2023), 6841–6853. https://doi.org/10.1523/JNEUROSCI.0930-22.2023

16. G. Drion, L. Massotte, R. Sepulchre, V. Seutin, How modeling can reconcile apparently discrepant experimental results: The case of pacemaking in dopaminergic neurons, *PLoS Comput. Biol.*, **7** (2011), 1002050. https://doi.org/10.1371/journal.pcbi.1002050

17. O. Waroux, L. Massotte, L. Alleva, A. Graulich, E. Thomas, J. F. Liégeois, et al., SK channels control the firing pattern of midbrain dopaminergic neurons in vivo, *Eur. J. Neurosci.*, **22** (2005), 3111–3121. https://doi.org/10.1111/j.1460-9568.2005.04484.x

18. R. Lyer, M. A. Ungless, A. A. Faisal, Calcium-activated SK channels control firing regularity by modulating sodium channel availability in midbrain dopamine neurons, *Nature*, **7** (2017), 5248. https://doi.org/10.1038/s41598-017-05578-5

19. C. C. Canavier, S. A. Oprisan, J. C. Callaway, H. Ji, P. D. Shepard, Computational model predicts a role for ERG current in repolarizing plateau potentials in dopamine neurons: Implications for modulation of neuronal activity, *J. Neurophys.*, **98** (2007), 3006–3022. https://doi.org/10.1152/jn.00422.2007

20. H. Ji, K. R. Tucker, I. Putzier, M. A. Huertas, J. P. Horn, C. C. Canavier, et al., Functional characterization of ether-à-go-go-related gene potassium channels in midbrain dopamine neurons-implications for a role in depolarization block, *Eur. J. Neurosci.*, **36** (2012), 2906–2916. https://doi.org/10.1111/j.1460-9568.2012.08190.x

21. A. A. Grace, B. S. Bunney, Induction of depolarization block in midbrain dopamine neurons by repeated administration of haloperidol: Analysis using in vivo intracellular recording, *J. Pharmacol. Exp. Ther.*, **238** (1986), 1092–1100. https://doi.org/10.1016/0160-5402(86)90023-9

22. A. A. Grace, D. L. Uliana, Insights into the mechanism of action of antipsychotic drugs derived from animal models: Standard of care versus novel targets, *Int. J. Mol. Sci.*, **24** (2023), 12374. https://doi.org/10.3390/ijms241512374

23. S. Nedergaard, J. A. Flatman, I. Engberg, Nifedipine- and omega-conotoxin-sensitive Ca2+ conductances in guinea-pig substantia nigra pars compacta neurones, *J. Physiol.*, **466** (1993), 727–747. https://doi.org/10.1113/jphysiol.1993.sp019742

24. O. Garritsen, E. Y. van Battum, L. M. Grossouw, R. J. Pasterkamp, Development, wiring and function of dopamine neuron subtypes, *Nature*, **24** (2023), 134–152. https://doi.org/10.1038/s41583-022-00669-3

25. S. W. Johnson, Y. N. Wu, Multiple mechanisms underlie burst firing in rat midbrain dopamine neurons in vitro, *Brain Res.*, **1019** (2004), 293–296. https://doi.org/10.1016/j.brainres.2004.06.022

26. D. J. Galtieri, C. M. Estep, D. L. Wokosin, S. Traynelis, D. J. Surmeier, Pedunculopontine glutamatergic neurons control spike patterning in substantia nigra dopaminergic neurons, *Elife*, **6** (2017), e30352. https://doi.org/10.7554/eLife.30352

27. N. Yu, K. R. Tucker, E. S. Levitan, P. D. Shepard, C. C. Canavier, Implications of cellular models of dopamine neurons for schizophrenia, *Prog. Mol. Biol. Transl. Sci.*, **123** (2014), 53–82. https://doi.org/10.1016/B978-0-12-397897-4.00011-5

28. R. D. Howell, S. Dominguez-Lopez, S. R. Ocañas, W. M. Freeman, M. J. Beckstead, Female mice are resilient to age-related decline of substantia nigra dopamine neuron firing parameters, *Neurobiol. Aging*, **95** (2020), 195–204 https://doi.org/10.1016/j.neurobiolaging.2020.07.025

29. J. Rinzel, A formal classification of bursting mechanisms in excitable systems, *Math. Top. Popul. Biol. Morphog. Neurosci.*, **519** (1987), 267–281. https://doi.org/10.1007/978-3-642-93360-8-26

30. B. Ibarz, J. M. Casado, M. A. F. Sanjuán, Map-based models in neuronal dynamics, *Phys. Rep.*, **501** (2011), 1–74. https://doi.org/10.1016/j.physrep.2010.12.003

31. Y. H. Qian, D. J. Zhang, Bursting oscillation and mechanism analysis of a class of Duffing-Van der Pol system with two excitation terms, *Eur. Phys. J. Plus*, **138** (2023), 1017. https://doi.org/10.1007/978-3-642-93360-8-26

32. R. Bertram, M. J. Butte, T. Kiemel, A. Sherman, Topological and phenomenological classification of bursting oscillations, *Bull. Math. Biol.*, **57** (1995), 413–439. https://doi.org/10.1007/BF02460633

33. N. Yu, C. C. Canavier, A mathematical model of a midbrain dopamine neuron identifies two slow variables likely responsible for bursts evoked by SK channel antagonists and terminated by depolarization block, *J. Math. Neurosci.*, **5** (2015), 1–19. https://doi.org/10.1186/s13408-015-0017-6

34. C. Knowlton, S. Kutterer, J. Roeper, C. C. Canavier, Calcium dynamics control K-ATP channel-mediated bursting in substantia nigra dopamine neurons: A combined experimental and modeling study, *J. Neurophys.*, **119** (2018), 84–95. https://doi.org/10.1152/jn.00351.2017

35. B. Lu, X. F. Jiang, Reduced and bifurcation analysis of intrinsically bursting neuron model, *Electron. Res. Arch.*, **31** (2023), 5928–5945. https://doi.org/10.3934/era.2023301

36. T. Carnevale, M. Hines, *The Neuron Book*, Cambridge University Press, 2017. https://doi.org/10.1017/CBO9780511541612

37. Origin. Available from: http://www.originlab.com .

38. G. Y. Zhou, T. Noto, A. Sharma, Q. Yang, K. A. G. Otárula, M. Tate, et al., HFOApp: A MATLAB graphical user interface for high-frequency oscillation marking, *eNeuro*, **8** (2021), 0509–0520. https://doi.org/10.1523/ENEURO.0509-20.2021

39. A. Dhooge, W. Govaerts, Y. A. Kuznetsov, MATCONT: A Matlab package for numerical bifurcation analysis of ODEs, *ACM Trans. Math. Software*, **29** (2003), 141–164. http://dx.doi.org/10.1145/779359.779362

40. R. Fitzhugh, Impulses and physiological states in theoretical models of nerve membrane, *Biophys. J.*, **1** (1961), 445–466. https://doi.org/10.1016/S0006-3495(61)86902-6

41. F. A. Carrillo, F. Verduzco, J. Delgado, Analysis of the Takens-Bogdanov bifurcation on m-parameterized vector fields, *Int. J. Bifurcation Chaos*, **20** (2010), 995–1005. https://doi.org/10.1142/S0218127410026277

42. Y. A. Kuznetsov, *Elements of Applied Bifurcation Theory*, New York: Springer-Verlag, 1998. https://doi.org/10.1007/b98848

AIMS Press